JOURNAL OF PROPULSION AND POWER
Vol. 27, No. 4, July–August 2011

Transient Three-Dimensional Side-Load Analysis of Out-of-Round Film-Cooled Nozzles

Ten-See Wang,* Jeff Lin,† Joe Ruf,† and Mike Guidos‡
NASA Marshall Space Flight Center, Huntsville, Alabama 35812

DOI: 10.2514/1.B34082

The objective of this study was to investigate the effect of nozzle out-of-roundness on the nozzle side loads generated during an engine start transient. The out-of-roundness could be the result of asymmetric loads induced by hardware attached to the nozzle, asymmetric internal stresses, and deformation induced by previous tests. The rocket engine studied encompasses a regeneratively cooled chamber and nozzle, along with a film-cooled nozzle extension. The computational methodology is based on an unstructured-grid, pressure-based computational fluid dynamics formulation and transient inlet boundary conditions from an engine system simulation. Computations were performed for engine startup with the out-of-roundness achieved by four different degrees of ovalization: one perfectly round, one slightly out-of-round, one more out-of-round, and one significantly out-of-round. The results show that the separation-line jump was the source of the peak side load for the first three configurations, with the peak side load increasing as the degree of out-of-roundness increased. For the significantly-out-of-round nozzle, the peak side load was reduced to a level comparable with that of the round nozzle, due to a splitting of the separation-line jump.

Nomenclature

C_1, C_2, C_3, C_μ	=	turbulence modeling constants, 1.15, 1.9, 0.25, and 0.09.
C_p	=	heat capacity
D	=	diffusivity
F_{yz}	=	integrated force in the lateral direction
H	=	total enthalpy
K	=	thermal conductivity
k	=	turbulent kinetic energy
L/S	=	ratio of long axis to short axis
Q	=	heat flux
T	=	temperature
t	=	time, s
u	=	mean velocities
V^2	=	$\sum u^2$
x	=	Cartesian coordinates or nondimensional distance
α	=	species mass fraction
ε	=	turbulent kinetic energy dissipation rate
θ	=	energy dissipation contribution
μ	=	viscosity
μ_t	=	turbulent eddy viscosity ($\rho C_\mu k^2/\varepsilon$)
Π	=	turbulent kinetic energy production
ρ	=	density
σ	=	turbulence modeling constants, 0.9, 0.9, 0.89, and 1.15 for Eqs. (2) and (4–6).
τ	=	shear stress
ω	=	chemical species production rate

Subscripts

r	=	radiation
t	=	turbulent flow
w	=	wall
∞	=	ambient

I. Introduction

NOZZLE lateral forces during transient operations, if not properly managed, are known to cause severe structural damages to the engine and its supporting flight hardware to almost all liquid rocket engines during their initial development [1–4]. For example, the J-2 engine had its gimbal block retaining bolts fail in tension [4], the space shuttle main engine (SSME) had a liquid hydrogen feed line fracture [2,4], and the Japanese LE-7A engine had its cooling tubes broken [3]. There likely have been many unreported incidents all over the world. Therefore, transient nozzle side load is considered a high-risk item and a critical design issue during any new engine development. For that reason, many research efforts [5–18] have been devoted to understanding side-load physics and their impact on the magnitude of side loads.

The Ares I upper-stage engine, the J-2X engine currently under development, is an evolved variation of two historic predecessors: the J-2, which propelled the upper stages of the Apollo-era Saturn IB and Saturn V rockets, and the J-2S, a derivative of the J-2 that was developed and hot-fire-tested but never flown. It is expected that the J-2X engine will experience side forces, like its predecessors J-2 and J-2S [1] or engines similar in film-cooling design, such as the LE-7A [3,13] and Vulcain engines. Tomita et al. [13] noted that the new design of LE-7A engine does not include the film-cooling design, because it led to a jump in the nozzle flow-separation line and produced the LE-7A's peak side loads [3,8]. The impact of side forces on J-2X engine structures is therefore a major concern for the nozzle designers and test engineers.

A computational fluid dynamics (CFD) methodology [7,8] has been used to calculate the J-2X flow evolution and resulting nozzle side loads under various operating conditions and environments. One of the potential issues currently being explored is the effect of nozzle deformation, or out-of-roundness of the nozzle. Liquid rocket engine nozzles, being large, relatively lightweight structures, are probably never truly round. The causes of out-of-roundness could be, but are not limited to, the asymmetric loads induced by other hardware attached to the nozzle, asymmetric material internal stresses induced

Presented as Paper 2010-6656 at the 46th AIAA/ASME/SAE/ASEE Joint Propulsion Conference, Nashville, TN, 25–28 2010; received 10 August 2010; revision received 6 January 2011; accepted for publication 8 January 2011.

*Aerospace Engineer, ER42, Fluid Dynamics Branch, Propulsion Structure, Thermal, and Fluids Analysis Division. Senior Member AIAA.

†Aerospace Engineer, ER42, Fluid Dynamics Branch, Propulsion Structure, Thermal, and Fluids Analysis Division.

‡Aerospace Engineer, ER21, Liquid Engine & Main Propulsion Systems Branch, Propulsion Systems Design & Integration Division.

in previous tests, and nozzle wall material deformation, such as creep, incurred in previous engine tests.

The current interest in the out-of-round nozzles comes from the fact that in a perfectly round nozzle, the nozzle side forces arise from asymmetric shock evolutions. Questions were therefore raised about the side-load characteristics of out-of-round nozzles. To gain insight into side-load characteristics of out-of-round nozzles, transient 3-D CFD analyses were performed of the J-2X nozzle flow during the engine startup process on ovalized nozzles. Four nozzles with different degrees of ovalization were used to study the effect of out-of-roundness: a perfectly round, or nominal, nozzle; a slightly ovalized nozzle; a more ovalized nozzle; and a significantly ovalized nozzle.

To the best of the authors' knowledge, this is the first analysis of the effect of nozzle deformation on side loads. Ostlund and Bigert [9] studied several nonround, polygon nozzles. Those polygon nozzles were not deformed nozzles, however, because they were specially designed as faceted nozzles to try to reduce nozzle side loads. The results of these computations are presented and discussed herein.

II. Computational Methodology

A. Computational Fluid Dynamics

The CFD methodology is based on a multidimensional, finite volume, viscous, chemically reacting, unstructured-grid, and pressure-based formulation. Time-varying transport equations of continuity, species continuity, momentum, total enthalpy, turbulent kinetic energy, and turbulent kinetic energy dissipation were solved using a time-marching subiteration scheme and are written as

$$\frac{\partial \rho}{\partial t} + \frac{\partial}{\partial x_j}(\rho u_j) = 0 \tag{1}$$

$$\frac{\partial \rho \alpha_i}{\partial t} + \frac{\partial}{\partial x_j}(\rho u_j \alpha_i) = \frac{\partial}{\partial x_j}\left[\left(\rho D + \frac{\mu_t}{\sigma_\alpha}\right)\frac{\partial \alpha_i}{\partial x_j}\right] + \omega_i \tag{2}$$

$$\frac{\partial \rho u_i}{\partial t} + \frac{\partial}{\partial x_j}(\rho u_j u_i) = -\frac{\partial p}{\partial x_i} + \frac{\partial \tau_{ij}}{\partial x_j} \tag{3}$$

$$\frac{\partial \rho H}{\partial t} + \frac{\partial}{\partial x_j}(\rho u_j H) = \frac{\partial p}{\partial t} + Q_r + \frac{\partial}{\partial x_j}\left(\left(\frac{K}{C_p} + \frac{\mu_t}{\sigma_H}\right)\nabla H\right) + \frac{\partial}{\partial x_j}\left(\left((\mu + \mu_t) - \left(\frac{K}{C_p} + \frac{\mu_t}{\sigma_H}\right)\right)\nabla(V^2/2)\right) + \theta \tag{4}$$

$$\frac{\partial \rho k}{\partial t} + \frac{\partial}{\partial x_j}(\rho u_j k) = \frac{\partial}{\partial x_j}\left[\left(\mu + \frac{\mu_t}{\sigma_k}\right)\frac{\partial k}{\partial x_j}\right] + \rho(\Pi - \varepsilon) \tag{5}$$

$$\frac{\partial \rho \varepsilon}{\partial t} + \frac{\partial}{\partial x_j}(\rho u_j \varepsilon) = \frac{\partial}{\partial x_j}\left[\left(\mu + \frac{\mu_t}{\sigma_\varepsilon}\right)\frac{\partial \varepsilon}{\partial x_j}\right] + \rho\frac{\varepsilon}{k}(C_1\Pi - C_2\varepsilon + C_3\Pi^2/\varepsilon) \tag{6}$$

A predictor–corrector solution algorithm was employed to provide coupling of the governing equations. A second-order central-difference scheme was employed to discretize the diffusion fluxes and source terms. For the convective terms, a second-order upwind total-variation-diminishing difference scheme was used. To enhance the temporal accuracy, a second-order backward-difference scheme was employed to discretize the temporal terms. Point-implicit method was used to solve the chemical species source terms. Subiterations within a time step were used for driving the system of second-order time-accurate equations to convergence. Details of the numerical algorithm can be found in [19–22].

An extended k-ε turbulence model [23] was used to describe the turbulence. A modified wall function approach was employed to provide wall boundary-layer solutions that are less sensitive to the near-wall grid spacing. Consequently, the model has combined the advantages of both the integrated-to-the-wall approach and the conventional law-of-the-wall approach by incorporating a complete velocity profile and a universal temperature profile [24]. A seven-species, nine-reaction detailed mechanism [24] was used to describe the finite rate, hydrogen/oxygen afterburning combustion kinetics. The seven species are H_2, O_2, H_2O, O, H, OH, and N_2. The thermodynamic properties of the individual species are functions of temperature. The multiphysics pertinent to this study have been anchored in earlier efforts, e.g., SSME axial force and wall heat transfer [19], SSME startup side load and dominant shock-breathing frequency [7], J-2X startup and shutdown side loads for a nozzlette configuration [8], nozzle film-cooling applications [25], and conjugate heat transfer [26].

B. Transient Startup Sequences

The engine startup and shutdown sequences are important drivers to the nozzle side-load physics [7,8]. The ramp rate of the pressure sequence generally determines the magnitude and duration of the peak side load. The temperature and species mass fraction sequences determine the extent of the combustion reactions that affect the magnitude and duration of the side loads. Another reason the temperature and species composition are important is that they largely determine the specific heat distribution, which affects the shock shape and impacts the side-load physics. Giving another example of the importance of the species composition, if excess fuel is dumped early in the transient, combustion waves could occur, which would add to the severity of the side load [7].

Transient system-level simulations provide the time histories of the aforementioned variables. The system-level simulations are a lumped control-volume analysis approach to model the network of components and subcomponents, in a rocket engine. Transient system-level modeling is therefore an important tool in the design and planning of sequencing the transient events of rocket engine operation. Figure 1 presents the inlet pressure and temperature time histories, and Fig. 2 shows the inlet species mass fraction time histories for the main combustion chamber (MCC) and the turbine exhaust gas (TEG) flows. TEG flow is used as film coolant for the J-2X nozzle extension and also provides a small benefit to engine thrust performance. The transient reactant composition obtained from system modeling was preprocessed with the Chemical

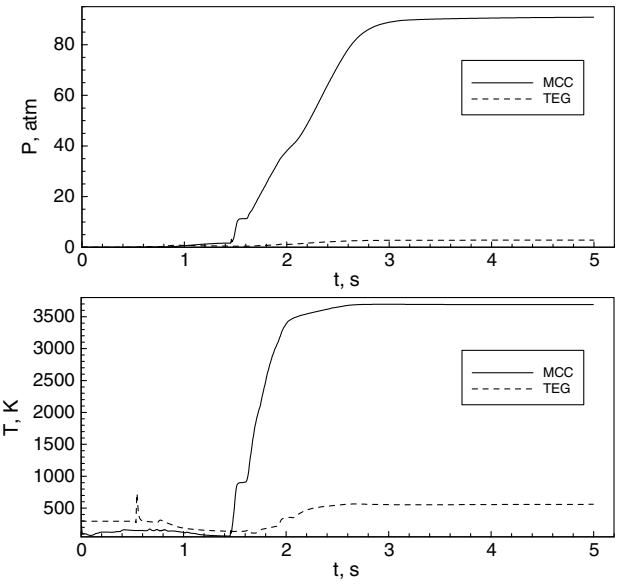

Fig. 1 Simulated inlet pressure and temperature histories for the main combustion chamber and turbine exhaust gas flows during the startup transient.

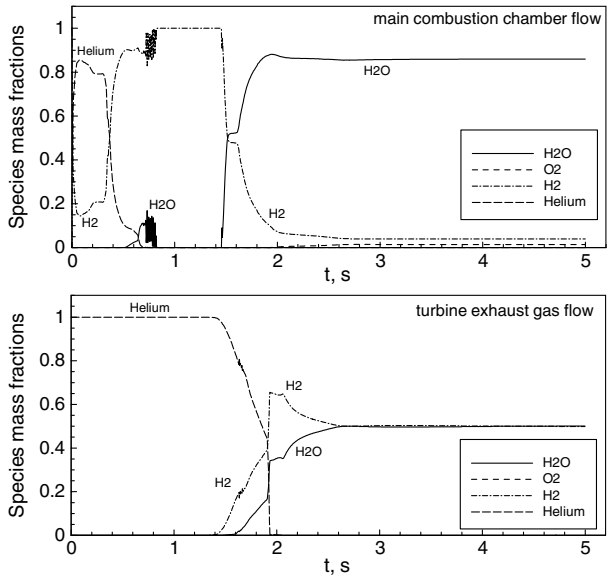

Fig. 2 Simulated inlet species mass fraction histories for the main combustion chamber and turbine exhaust gas flows during the startup transient.

Equilibrium Calculation program [27], assuming the propellants were ignited to reach equilibrium composition immediately downstream of the injector faceplate or turbine exhaust manifold inlet boundary. Figure 1 shows that the majority of the increase in MCC pressure and temperature occurs between 1.4 and 3 s. Also, it can be seen from Fig. 2 that immediately following the start command, helium enters both the MCC, as a purge flow, and the TEG chamber, initially as a purge flow, but then to assist the turbopump spinup.

Helium is initially present in the MCC nozzle flowfield, due to purges used during the early stages of the start sequence from the main injector and gas generator (GG) TEG flowpath. This helium in the MCC is pushed out as the initial fuel flow and igniter low-flow/low-pressure combustion flows become established to the MCC, as shown in the transient MCC species mass fraction profile in Fig. 2. The main fuel valve is opened first, to establish the initial fuel flow in the main fuel injector and MCC augmented spark igniter (ASI), ensuring a fuel-rich start of the MCC and safely allowing the J-2X fuel turbopump to start ramping up. To provide the initial breakaway momentum to the pumps and initiate higher pump flow rates, a helium-spin-assist system is used to inject a short-duration ($\sim$1.4 s), high-pressure, high flow of helium gas into the turbines. Simultaneous with the initiation of the helium-spin-assist system, the main oxidizer valve is opened to allow priming of the downstream oxidizer system with purely liquid oxidizer. Also in this same period, the low-flow oxidizer valve is opened to allow flow to the MCC ASI and initiate low-flow/low-pressure combustion in this early time frame. It is during this spin-start system operation, before any significant flow through the MCC main injector, that the nozzle side loads hit a peak magnitude (at 0.80–1.10 s).

As the spin-start system is initiated, the helium exhausts through the TEG (after passing through the fuel and oxidizer turbines) and into the nozzle extension. As already mentioned, this discharge of helium-spin gas from the TEG into the nozzle flowfield occurs before any significant flow through the main injector, thus promoting the possibility of loading of the nozzle asymmetrically. As this spinup gas flow decays, the GG fuel and oxidizer valves are opened, further accelerating the pumps and both fuel and oxidizer flows throughout the engine. However, this transition of pump-driving fluid from spin-assist helium to GG-generated hot gas is not instantaneous, and there is a period of time during which engine system flows and pressures decay.

During this power-transition period, the main injector oxidizer dome primes with liquid oxygen, which is a crucial step in starting the engine safely, as the oxidizer flow to the MCC then becomes more controllable and predictable, increasing the likelihood for stable MCC combustion as engine power is sharply increased. As the flow of oxidizer in the main oxidizer injector initiates and then primes with liquid, the MCC pressure rises sharply to the first small plateau in the $\sim$1.4–1.6 s time frame, as shown in the transient MCC pressure profile in Fig. 1. The rise in MCC pressure correspondingly causes a decrease in fuel system flow and pressure to the MCC, thus causing the brief stagnation or plateau in MCC pressure.

Once the GG combustion flow begins to build (which exhausts through the TEG flowpath), the pumps accelerate, and their respective propellant flows to the MCC also accelerate, driving the engine system to full-power (or main-stage) conditions throughout. After the start of the GG and the hot combustion gas flow rapidly builds, the remaining helium in the TEG flowpath is completely pushed out, as shown in the transient TEG species mass fraction profile in Fig. 2. Essentially, engine steady-state operation is attained approximately within 4.5 to 5.0 s after the engine start command is received, although thermal equilibrium effects between the propellant flows and the metal mass within the engine prevent flows from completely steadying until a much later time.

These helium flows dilute the fuel concentration in the early startup process. It was found in an earlier study [8] that a combination of the fuel dilution and a shorter ramp time than that of the SSME eliminated the occurrence of potentially hazardous combustion waves [7]. It should be noted that the startup sequences shown in Figs. 1 and 2 are different from those shown in an earlier study [8]; e.g., the temperature spike during the earlier startup transient [8] was eliminated.

III. Computational Grid Generation

Figure 3 shows the grid layout on the surface of the J-2X engine hardware contained in the computational domain. The computational domain for this J-2X out-of-round nozzle side-load investigation includes the MCC, the nozzle, the turbine exhaust manifold (TEM), the nozzle extension, and a freestream region surrounding the engine. The TEM is a nonsymmetrical torus that supplies the TEG to the nozzle extension nonuniformly around the circumference of the nozzle extension. The computational domain of the TEM consists of an inlet duct and the aforementioned torus in which the TEG flow splits, flowing around the torus and subsequently into the nozzle extension. The exit of the TEM is a narrow annular slot of constant area through which the TEG exhausts supersonically onto the nozzle-extension inner wall. A separate steady-state main-stage analysis

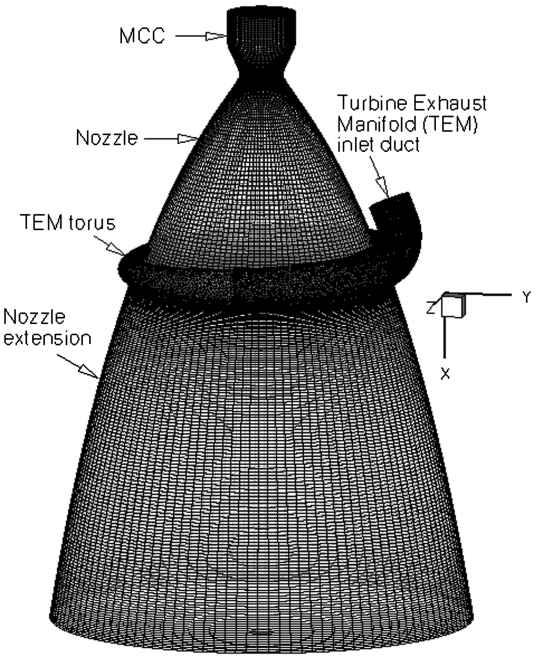

Fig. 3 Grid layout of the nominal geometry.

with this TEM configuration indicated that it produces a 9%-higher-than-uniform mass flow into the nozzle extension in the region under the TEM inlet duct.

The general procedure of the grid generation follows that of the SSME side-load study [7] and the previous J-2X side-load study [8] by rotating an axisymmetric grid first without the TEM. The TEM grid was constructed separately, as it is asymmetric to the central axis. The grid was completed by merging these two grids at the TEG exit through one-to-one grid connectivity. The software package GRIDGEN [28] was used to perform the grid generation. The general layout of the outer boundaries and the wall boundaries of the MCC, nozzle, TEM, and nozzle extension are similar to those of the previous J-2X side-load study and are described in detail in [8]. Figure 4 shows a close-up view of the grid for the MCC, nozzle, and TEM without the nozzle extension. The TEM's structural ribs were modeled and are visible at the bottom of the TEM in Fig. 4.

A grid-study procedure was developed for transient nozzle side-load calculations in earlier studies [7,8,19]. It was based on the recognition that a conventional grid study would be computationally prohibitive for side-load investigations because of the need for a large amount of computer resources, due to the requirements of a full 360 deg of three-dimensional domain, turbulent reacting flow, and computation of 3 to 5 real seconds of engine transient operation. Knowing that peak side force is usually a small percentage of the axial force, the grid study was performed on a steady-state axial-force calculation, based on the assumption that if the grid density is adequate for the calculated steady-state axial force, then it is adequate for the calculated transient side forces. The grid study started with an axisymmetric grid first and included the 3-D grid. The 3-D grid is achieved by rotating the axisymmetric grid 360 deg to ensure that the asymmetric flow comes from the transient physics and not the asymmetric grid. It is critical that the grid density for the axisymmetric grid is adequate. Otherwise, the rotated 3-D grid will have a difficult time matching the desired axial force [19]. From the results of previous studies on the SSME transient startup [7] and the transient startup and shutdown of the J-2X engine [8], a circumferential division number of 72 was found to be adequate in capturing the major side-load physics such as the shock transitions, shock breathing across the nozzle lip, and separation-line jump. More important, the SSME side load computed for those major physics agreed reasonably well with those of hot-fire-test SSME measurements [7]. In addition, the computed dominant oscillation frequency during the shock breathing also agreed well with test

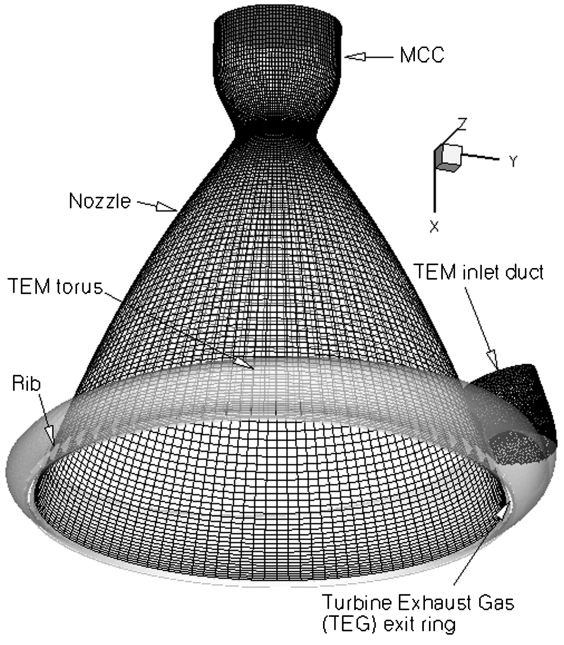

Fig. 4 Close-up view of the turbine exhaust manifold.

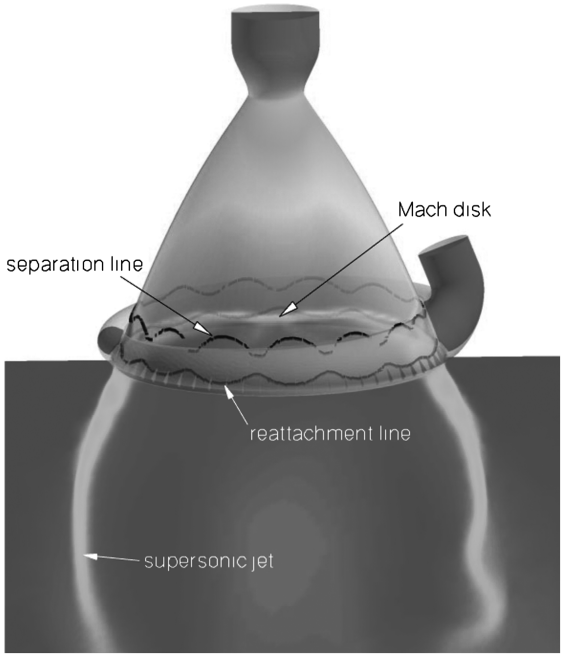

Fig. 5 Separation and reattachment lines, and Mach number contours for a nominal stub nozzle at 1.82 s into startup transient at sea level.

measurements [7]. This grid-study procedure was therefore demonstrated to be sufficient for nozzle side-load study.

In this effort, because of increased computational resources available, the circumferential division number was increased to 120, or a 67% increase over the previous efforts [7,8]. To test the effect of the increased circumferential grid resolution, a separate transient startup calculation of the J-2X stub nozzle at sea level was performed to see if teepees can be captured. Teepees are formations of conical shocks that occur near the nozzle lip and have been observed during hot-fire tests. These were first described by Nave and Coffey [1] during J-2S engine tests and are often observed during SSME startup transients. They usually occur during the shock-breathing mode [7] when the shock foot moves in and out of the nozzle lip. A stub nozzle without the nozzle extension was chosen because a shorter nozzle would flow full faster. The resulting Mach number contours show that shock breathing occurred between 1.775 and 1.94 s and teepees were seen between 1.775 and 1.845 s Fig. 5 shows the captured teepees with separation and reattachment lines at 1.82 s into the startup transient. The total number of teepees captured in this time slice is 13, which is higher resolution over the three–five teepeelike structures captured in previous studies [7,8]. This result shows one aspect of improvement in capturing the transient nozzle physics through the increased circumferential grid resolution.

For the out-of-round nozzles, the out-of-roundness was imposed by ovalizing the entire grid (from the injector face to the nozzle-extension exit) by varying the ratio of the long axis to the short axis. Figure 6 shows a cross-sectional view of the four nozzle surfaces used in this study. The nominal, or perfectly round, case has a long axis to short axis (L/S) ratio of unity; the slightly-out-of-round case has an L/S ratio of 1.0086; the more-out-of-round case, has an L/S ratio of 1.0346. Finally, the L/S ratio of the significantly-out-of-round case is unrealistically high at 1.4400. It is estimated that the slightly-out-of-round and the more-out-of-round cases are the most likely scenarios, and the significantly-out-of-round nozzle is intended as a hypothetical case that serves as the limit for out-of-roundness.

The L/S ratios of 1.0086 and 1.0346 were implemented to produce a deformation of ± 0.25 and ± 1.0 in the long and short axes at the exit plane of the nozzle extension. The same scaling was applied to the entire engine domain; therefore, the nozzle throat and TEM exit ring areas and shapes were altered. For the slightly- and more-out-of-round cases, the changes in these areas are assumed to have a small effect on the mass flow distribution and nozzle

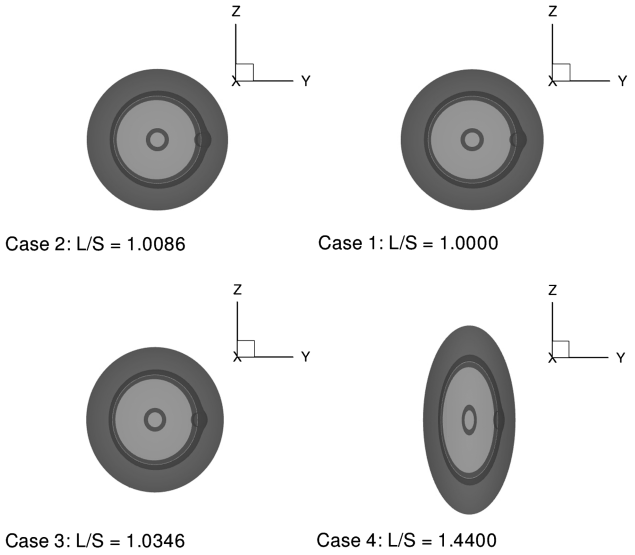

Fig. 6 Cross-sectional view of the ovalized nozzles.

flow-separation development. For the L/S ratio of 1.44, the same assumption cannot be made. The changes in the nozzle throat, nozzle wall, and TEM exit ring geometries were too large. But, again, the $L/S = 1.44$ was a hypothetical study case.

Because of the shape of the TEM structure, it was assumed that the long axis of the imposed ovalization was aligned with the z coordinate. The short axis was aligned with the y coordinate, in line with the TEM inlet, as indicated in Fig. 6. The total number of cell volumes was 4,421,166 for all four cases. The total number of cells used in this study is higher than the 2,058,192 cells used in the previous J-2X side-load study [8] and much higher than the 1,275,120 cells used in the SSME benchmark [7]. It is noted that although the cross-sectional flow areas of the four nozzles do not have to be the same, it is further assumed that those are the same, such that the results are compared on an equal-flow-area basis.

IV. Boundary and Inlet Conditions

Since J-2X is the upper-stage engine of the Ares vehicles, fixed freestream boundary conditions were set corresponding to 100,000 ft. Time-varying inlet flow boundary conditions were used at the MCC and TEG inlets. These inlet flow properties (obtained from the system-level simulations) were the time-varying total pressure, temperature, and reactant compositions, as shown in Figs. 1 and 2. For engine startup computations, the thermal wall boundary condition was initially adiabatic. When the startup transient simulation reached 1.4 s, the point where the MCC pressure started to ramp up, wall temperature profiles obtained from a separate steady-state calculations were imposed onto the MCC and nozzle wall. The nozzle extension and TEM walls remained adiabatic (discussed in [7,8]).

Table 1 Run matrix

Case	Description	L/S ratio	Deformation, in.
1	Nominal (perfectly round)	1.0000	±0.00
2	Slightly out-of-round	1.0086	±0.25
3	More out-of-round	1.0346	±1.00
4	Significantly out-of-round	1.4400	±11.6

V. Results and Discussion

The computations were performed on a clustered machine using 20 to 24 processors. The processors used are dual-core AMD Opteron processor clocked at 2405 MHz. The computational cost was estimated as 5.8759E–6CPUs/step/cell/processor. For these transient computations at 100,000 ft, because the combustion reaction rates at such low backpressures are slow (compared with the rates at sea level), a global time step of 10 μs was used throughout the computations. These global time steps used correspond to Courant–Friedrichs–Lewy numbers ranging approximately from 0.1 to unity. For a typical 2 s simulation, the total number of flow steps is 200,000. The run matrix of the four cases is shown in Table 1. The result of the nominal case will be discussed first, followed by those of the three out-of-round cases.

A. Nominal Case

Figure 7 shows the computed J-2X side-load history during engine startup transient for the perfectly round case. Major startup physics and the timeline of their occurrence and duration are indicated at the top of the figure. A brief description of the time-evolving physics is in order. As indicated in Fig. 7, the exhaust plume of the transient startup begins as a subsonic core jet. As the chamber pressure increases, the core jet flow strengthens. When the core jet becomes supersonic, a Mach disk develops near the throat at around 0.40 s. Because of wall friction, this initial Mach disk flow is separated from the nozzle wall from the throat down. The combination of this flow-separation pattern and the associated shock structure of the Mach disk flow is named the free-shock separation (FSS) [1], because the supersonic jet stemming from the triple point is flowing freely away from the wall. As this Mach disk flow advances downstream, the size of the Mach disk grows as the nozzle flowing area increases. At about 0.65 s into the engine start, the TEG flow begins to emerge from the TEG exit ring into the nozzle extension.

As described earlier, at the main stage, this TEM configuration produces a 9%-higher-than-uniform mass flow distribution under the inlet. However, early in the startup transient, the TEM exit is more nonuniform, producing a localized pumping effect. In addition, since the ambient pressure at 100,000 ft is lower than that of the total pressures of the core and TEG flows, the external environment behaves like a vacuum pump. These pumping effects exacerbate the TEG flow imbalance, which draws the core flow's supersonic jet toward the TEM inlet duct side of the nozzle, forming an asymmetric Mach disk flow with a slanted separation line, as shown in the snapshot at 0.85 s in Fig. 8. This phenomenon is unique to this TEM configuration during startup and is named the *asymmetric TEG*

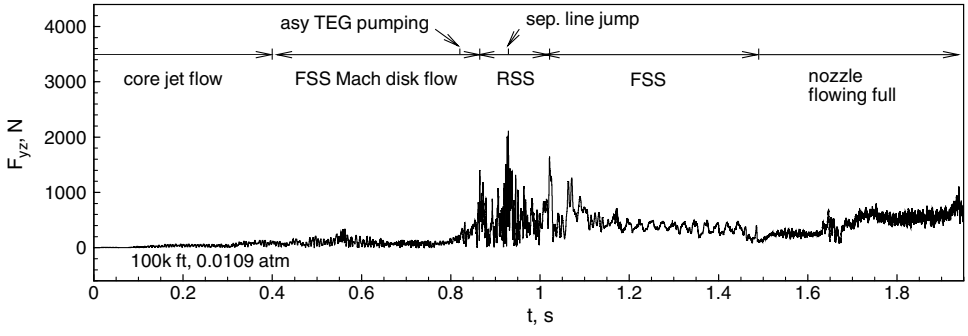

Fig. 7 Computed side-load history during startup for the nominal or perfectly round case.

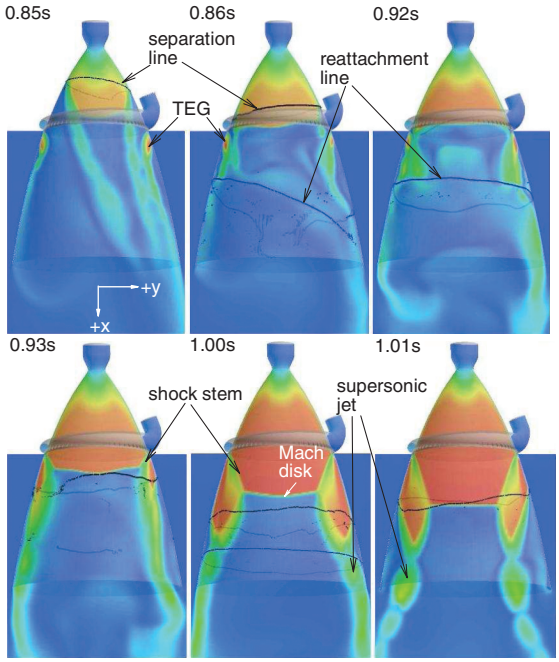

Fig. 8 Mach number contours on *xy* plane at selected time slices for the nominal case.

pumping herein. As a result, this phenomenon helps the asymmetric FSS Mach disk flow transiting into an asymmetric restricted-shock separation (RSS) Mach disk flow, generating the first local peak side load (at about 0.865 s, in Fig. 7). At 0.86 s in Fig. 8, the core flow's supersonic jet is merging with the TEG flow, forming an RSS flow pattern. In an RSS flow pattern, first observed and reported during J-2 and J-2S tests, the entire supersonic jet is attached or restricted to the nozzle wall [1].

At this time, the rear shock stem is quickly approaching the TEG exit ring, which is composed of a small base, or a backstep formation, between the nozzle contour and the TEG exit ring. As one would expect, when the rear shock stem jumps over the base and meets with the flowing TEG flow, a significant disturbance would be imposed onto the Mach disk flow. The snapshot for 0.92 s in Fig. 8 shows the shock stem of the RSS Mach disk flow just before this jump. By 0.93 s into the startup transient, the rear shock stem (i.e., the separation line on the wall) had jumped over the TEG exit ring and generated the peak side load of 2114 N. The 0.93 s snapshot in Fig. 8 shows a disturbed Mach disk flow right after the jump.

This separation-line-jump phenomenon was first reported by Watanabe et al. [3] as a *separation-point jump* during LE-7A engine tests. Later, Wang and Guidos [8] captured it computationally in J-2X transient simulation. Since the separation-line jump always produces a peak side load, it is considered the critical side-load physics for round film-cooled nozzles. Tomita et al. [29] noted that higher step height exaggerates the effect of separation-line jump. After 0.93 s the Mach disk flow continued its downstream movement, as shown in the 1.0 s snapshot. Subsequently, the RSS Mach disk flow transitioned back to an FSS Mach disk flow at about 1.01 s, generating another local peak side load. This FSS Mach disk flow oscillated several more times in the nozzle and eventually left the nozzle at around 1.49 s.

B. Out-of-Round Cases

Since nozzle side forces are caused by asymmetric flows or, specifically, asymmetric shock formations caused by major side-load physics during the transient process (e.g., combustion wave, FSS-to-RSS transition and vice versa, shock breathing at the lip, and jump of the separation line), it is anticipated that any further changes in operation or configuration that causes asymmetric flow would exacerbate the situation. As a case in point, the biased TEG flow distribution from the TEM is an example. It induces the asymmetric TEG pumping of the core flow, resulting in more severe asymmetric shock formation and higher peak side loads than the simulations with a symmetric TEG flow injection [8]. Nozzle out-of-roundness is another configuration change. It is expected that higher degrees of out-of-roundness, measured by the L/S ratio, will lead to higher peak side loads.

Figure 9 shows the computed side-load history and the timeline of the major physics for the slightly-out-of-round case, with a small L/S ratio of 1.0086, or a ± 0.25 in. deformation at the end of the nozzle extension. This case represents a permanent nozzle deformation due to internal stresses accumulated in previous tests or due to

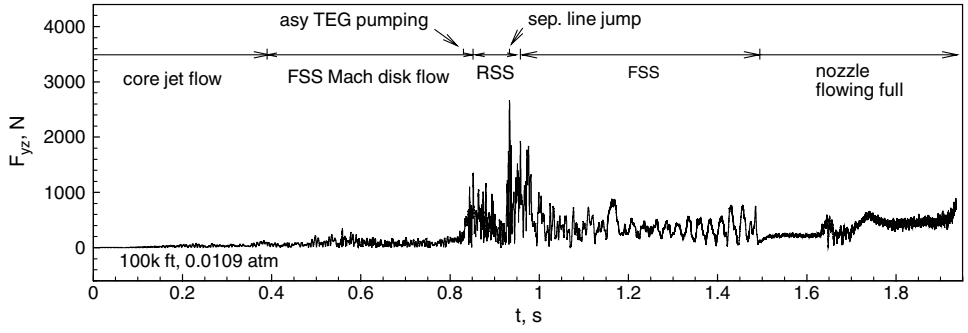

Fig. 9 Computed side-load history during startup for the slightly-out-of-round case ($L/S = 1.0086$).

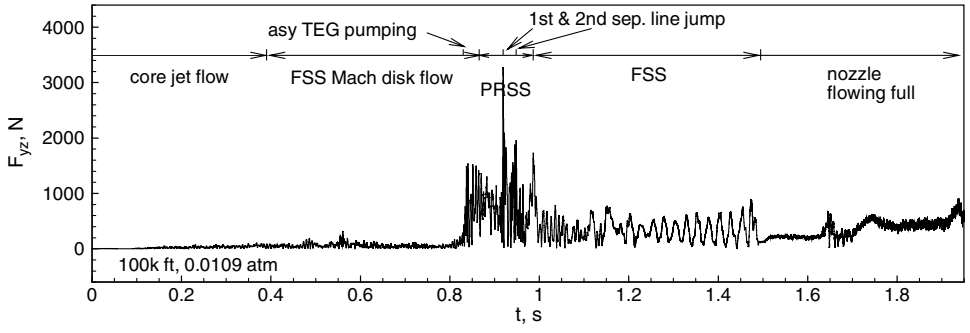

Fig. 10 Computed side-load history during startup for the more-out-of-round case ($L/S = 1.0346$).

asymmetric loads induced by hardware attached to the nozzle. Since the out-of-roundness is quite small, all the major side-load physics that occurred in the nominal case also happened in this slightly-out-of-round nozzle. Figure 9 shows the asymmetric TEG pumping, FSS-to-RSS transition, separation-line jump, and RSS-to-FSS transition. More important, the peak side load was also caused by the separation-line jump and its magnitude increased 26% to 2688 N. It is noted that the slightly-out-of-round nozzle caused the RSS to start and end slightly earlier than the perfectly round case. This is because in the slightly-out-of-round case, the TEG flow is slightly more uniform than that of the perfectly round case during the TEG pumping phase. As a result, the supersonic jet of the Mach disk flow was pumped more uniformly, and the FSS-to-RSS transition started slightly earlier for the slightly-out-of-round case. Subsequently, the RSS-to-FSS transition also started slightly earlier and the time span of RSS for the slightly-out-of-round case was slightly shorter than that for the perfectly round case.

Figure 10 shows the computed side-load history and the associated major physics for the more-out-of-round case. With a slightly larger L/S ratio of 1.0346 (a ± 1 in. physical deformation), such an out-of-roundness is also a likely scenario when there are internal stresses built up through many hot-fire tests. By comparing the major physics indicated in Fig. 10 with those of Figs. 7 and 9, it can be seen that all the major physics are still present with two differences. First, after the asymmetric TEG pumping, instead of FSS-to-RSS transition, there was an FSS-to-partial RSS (PRSS) transition, and instead of having one notable separation-line jump, the current case had two distinctive separation-line jumps. PRSS is a Mach disk flow-separation pattern between that of an FSS and an RSS Mach disk flow patterns. That is, the supersonic jet is only partially attached to the nozzle-extension wall. PRSS was first captured computationally in the unsteady simulations of LE-7, LE-7A, and CTP50-R5-L nozzles by Wonezawa et al. [30] and later captured by Wang [7] in the transient startup computation of an SSME nozzle.

These differences may be explained by examining time slices of Mach number contours in Fig. 11. For each time slice, two pictures are shown. The picture on the left-hand side is the Mach number contours on the x–y plane, and that on the right-hand side is the Mach number contours on the x–z plane. The x–y plane views the short-axis side (or narrower dimension) of the ovalized nozzle, and the x–z plane views the long-axis side (or wider dimension) of the ovalized nozzle. The difference in the nozzle's dimensions is not obvious in this image, since a deformation of ± 1 in. is difficult to see.

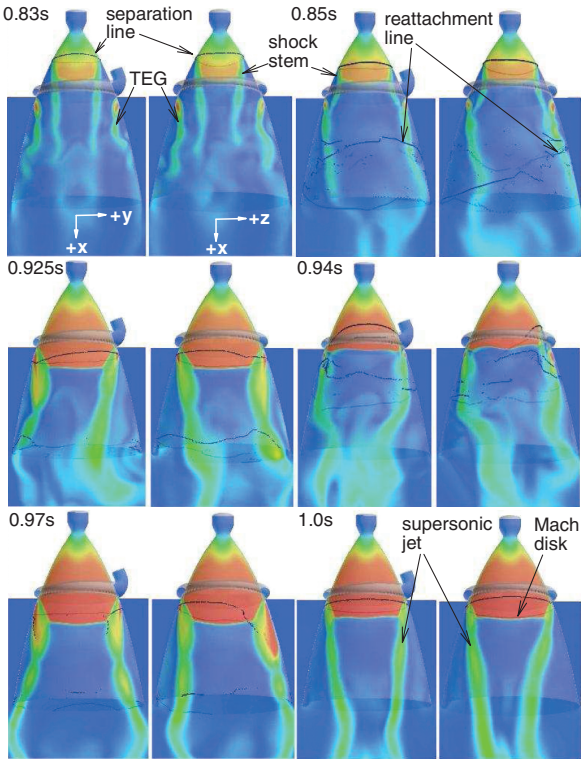

Fig. 11 Mach number contours at selected time slices for the more-out-of-round case.

In Fig. 11, at 0.83 s into the startup transient, the core flow's supersonic jet of the FSS Mach disk flow is experiencing the effect of pumping from the TEG flow. At 0.85 s, the core flow's supersonic jet merges with the TEG flow to create a PRSS flow. The x–y plane and x–z plane views show that the supersonic jet is bending into the quadrant of the nozzle on the TEM inlet duct side. The first separation-line jump happened at around 0.919 s. The disturbance to the Mach disk flow generated a peak side load of 3275 N: a 55% increase over that of the nominal case. The aftermath can be seen from the snapshots for 0.925 s, where there are disturbed separation and reattachment lines, along with a wildly swaying supersonic jet. In addition, the disturbance is so large that the rear shock stem retracted well back up into the nozzle, as shown from the partial and asymmetric separation line at 0.94 s. The partial reattachment line is also quite messy.

A second separation jump occurred at about 0.948 s, generating a lower side-load magnitude of 1960 N. At 0.97 s, the PRSS Mach disk flow still experiences the effect of second separation-line jumps, with fairly irregular separation and reattachment lines. The PRSS then transitioned to FSS at about 0.987 s and generated a side load of 1733 N. After that transition, the Mach disk flow returned to being normal to the nozzle centerline, as indicated by the snapshot taken at 1.0 s.

So far, with the increasing degree of out-of-roundness and the resulting enhanced asymmetric flow, the peak side loads have increased. One might expect that the peak side load of the significantly-out-of-round case would follow this trend and increase significantly more. Instead, the computed peak side load for the significantly-out-of-round case (Fig. 12) was only slightly higher than that of the nominal case. In addition, the peak side load was not generated by the separation-line jump (as with the other three cases), but from the FSS-to-RSS transition.

This counterintuitive result is explained with snapshots of the Mach number contours showing the major side-load physics (Fig. 13). As presented earlier in Fig. 11 for the more-out-of-round case, with each time slice, two views are shown: one for the x–y plane and another for the x–z plane. It is now obvious that x–y plane views of the nozzle show the short-axis side and the x–z plane views show the long-axis side. This significant change in the wall nozzle geometry altered the nozzle contour and the resulting expansion along it. The axial distribution of pressure on this nozzle contour would vary significantly with azimuth, decreasing more quickly with axial station on the long axis than on the short axis. The result is that the separation location varied with azimuth in the nozzle, producing the highly curved separation lines visible in the 0.70 s snapshots (upper left of Fig. 13). In fact, the separation line at 0.7 s is shaped like a sickle that bent downward on both ends of the short axis. The core flow supersonic jet in the x–z plane also developed a preference for the $+z$ direction.

At 0.88 s the FSS Mach disk flow transitioned to PRSS Mach disk flow. That disturbance moves the originally upward-bending separation line on the negative z coordinate side downward, thus severely distorting the Mach disk shape on the x–z plane, as shown in Fig. 13. This shock transition generated the peak side-load magnitude of 2171 N. Note that the Mach disk shape on the x–y plane appears to be stable and not disturbed. A flow-separation pattern such as that in the x–z plane alternated side to side and between PRSS and RSS until about 0.91 s. At about 0.91 s the first half of the separation line began to jump across the TEG exit ring and appears to have jumped by 0.915 s. This first half of the separation-line jump occurred at about 0.914 s and generated a side load of 1814 N, lower than that of the peak side-load magnitude of 2171 N, which was due to the FSS-to-PRSS transition.

The Mach number contours at 0.915 s (on the x–z plane in Fig. 13), right after the jump of the first half of the separation line, show the disturbed separation and reattachment lines and the Mach disk. Note

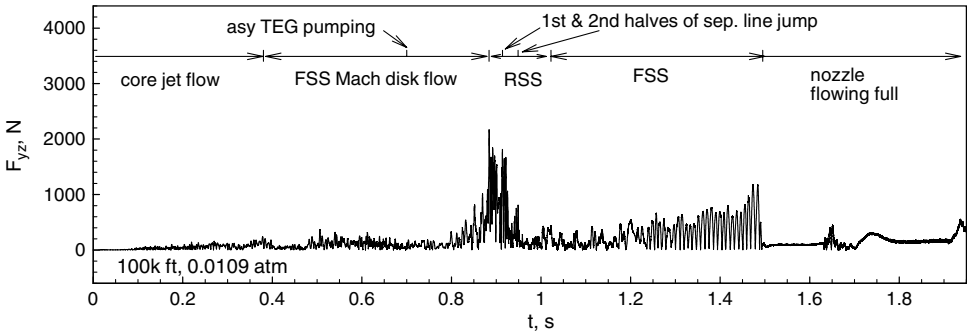

Fig. 12 Computed side-load history during startup for the significantly-out-of-round case ($L/S = 1.4400$).

that two separation lines are shown in the 0.91 and 0.915 s snapshots. The lower ones illustrate the TEG flow separation, which did not contribute significantly to side loads, because it never jumped. It is the part associated with the two ends of the upper separation line on the x–y plane that had jumped. The part (or two ends) of the upper separation line on the x–z plane was still up in the nozzle, above the plane of the TEG inlet ring, as shown in the 0.915 s snapshot in Fig. 13.

The second half of the separation-line jump, or the rest of the upper separation line on the two ends of x–z plane, occurred at about 0.949 s and generated a side load of 806 N. This was a lower side load than that from the first-half jump, because most of the upper separation line had already passed the TEG exit ring. The Mach number contours at 0.95 s into the startup transient, shown in Fig. 13, illustrate a more stable RSS flow pattern occurring right after the second half of the upper separation-line jump, although the separation and reattachment lines still look irregular at that time. Note that the upper separation line that jumped has disappeared, because the rear shock stem has merged with the TEG flow and the upper flow-separation zone was eliminated.

The RSS-to-FSS transition occurred at about 1.02 s, which generated a small side load of 436 N, and was the last of the major side-load physics. After that transition the flow was stable with the Mach number contours, like those shown for 1.035 s into the startup transient. The Mach disk appears to be normal to the nozzle axis on both planes, and the separation lines finally appear to be closer to the regular shape.

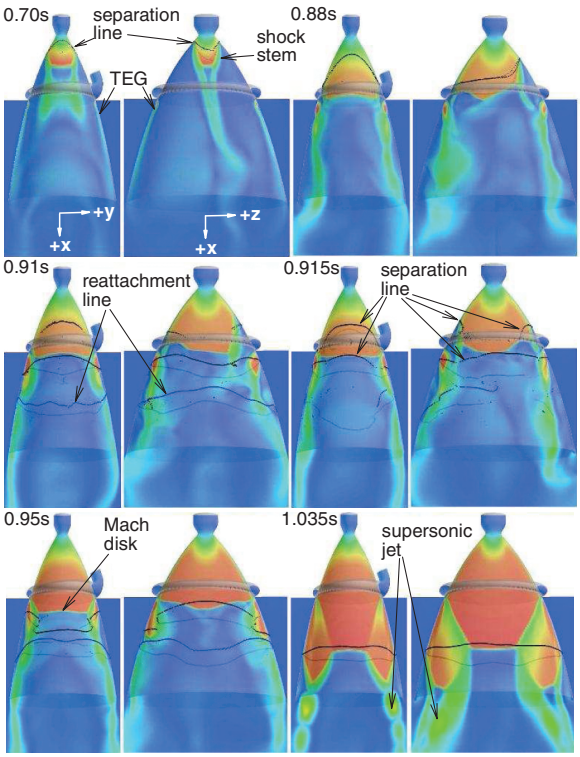

Fig. 13 Mach number contours of selected time slices for the significantly-out-of-round case.

Table 2 Comparison of the computed peak side loads

Nozzle shape	Peak F_{yz}, N	Physics
Perfectly round	2114	Separation-line jump
Slightly out-of-round	2668	Separation-line jump
More out-of-round	3275	Separation-line jump
Significantly out-of-round	2171	FSS-to-PRSS transition

A comparison of the peak side-load magnitudes, along with the associated side-load physics, is shown in Table 2. In summary, the peak side load increased progressively with the slightly- and more-out-of-round cases during the separation-line jump. However, there was an unexpected side-force stabilizing effect found during the transient startup of the significantly-out-of-round case. It is attributed to the large change in nozzle wall contour, which causes the separation line to move downstream faster in the two ends of the x–y plane than those in the x–z plane, resulting in a sickle-shaped separation line. The end result is that the usual physics that produce the peak side (the separation-line jump) for the perfectly round, the slightly-out-of-round, and more-out-of-round geometries were now weakened by splitting it into two parts. The faster-moving part of the separation line (associated with the two ends of the short-axis side) jumped first, and the slower-moving part of the separation line (associated with the two ends of the long axis) jumped second. This splitting of the separation-line jump was responsible for the peak-side-load reduction for the significantly-out-of-round case.

As mentioned earlier, Ostlund and Bigert [9] tested several nonround, or polygon, nozzles at sea level. The goal of the polygon nozzle design was to reduce, relative to a round nozzle, the first side-load peak that stemmed from the transition between FSS and RSS. The transition between FSS and RSS is said to be the critical side-load physics for Vulcain-type nozzles. They reported that the goal was achieved and attributed the reduction to three possible mechanisms. One of the mechanisms relevant to the current study is that the polygon corners acted as a kind of structure-breaker, splitting the flow-separation pattern in the azimuthal direction. This mechanism, splitting the separation line, is similar to that seen in the significantly-out-of-round nozzle and provides some experimental evidence that this flow pattern is credible. Therefore, it is concluded that the splitting of the flow separation (separation line) was the mechanism responsible for the reduction of side load for the significantly-out-of-round J-2X nozzle. Note that there are two aspects to this mechanism: the would-be peak-side-load physics were not only split in space, but were also split in time.

VI. Conclusions

Three-dimensional numerical simulations were performed to determine the effect of nozzle deformation on the nozzle's side loads during engine start transient for a film-cooled nozzle. Four amounts of deformation were simulated with different degrees of ovalization

of the entire flowpath: a nominal (round) nozzle, a slightly-out-of-round nozzle, a more-out-of-round nozzle, and a significantly-out-of-round nozzle. It was found that the rapid movement of the separation line, or its jump, over the TEG exit ring was the flow physics that induced the peak magnitude of nozzle side loads for the round, slightly-out-of-round, and more-out-of-round geometries and that the peak side load increased as the degree of out-of-roundness increased.

For the significantly-out-of-round case, a side-force stabilizing effect was discovered: the change in the nozzle wall contour caused the separation line to reach to TEG exit ring at different times. As a result, the separation-line jump was split into two parts: the fast-moving part of the separation line associated with the two ends of the short axis jumped first, and then the slow-moving part of the separation line jumped second. The peak magnitude was reduced, because the jump in the separation was split in both space and time. The peak side-load magnitude for the significantly-out-of-round case was reduced to a level comparable with that of the nominal, round nozzle. This peak-side-load reduction mechanism, splitting the peak-side-load physics in azimuth, is consistent with experimental results reported for nonround, polygon nozzles.

Acknowledgments

This study was partially supported by the J-2X Engine Program at MSFC. The lead author wishes to thank Mike Shadoan for his support of the task and James Beck of Pratt-Whitney Rocketdyne for his interest in this task. The fourth coauthor wishes to thank Duc Nguyen and Danny Woo of Pratt-Whittney Rocketdyne for providing the engine design and transient sequencing information necessary to create the MSFC J-2X engine system model.

References

[1] Nave, L. H., and Coffey, G. A., "Sea Level Side Loads in High-Area-Ratio Rocket Engines," AIAA Paper 73-1284, Nov. 1973.

[2] Cikanek, H. A., "Characteristics of Space Shuttle Main Engine Failures," AIAA Paper 87-1939, June 1987.

[3] Watanabe, Y., Sakazume, N., and Tsuboi, M., "LE-7A Engine Nozzle Problems During the Transient Operations," AIAA Paper 2002-3841, July 2002.

[4] Shi, J., "Rocket Engine Nozzle Side Load Transient Analysis Methodology—A Practical Approach," AIAA Paper 2005-1860, April 2005.

[5] Hagemann, G., Terhardt, M., Frey, M., Reijasse, P., Onofri, M., Nasuti, F., and Ostlund, J., "Flow Separation and Side-Loads in Rocket Nozzles," *4th International Symposium on Liquid Space Propulsion*, March 2000, DLR Lampoldshausen, pp. 1–19.

[6] Ruf, J., McDaniels, D. M., and Brown, A. M., "Nozzle Side Load Testing and Analysis at Marshall Space Flight Center," AIAA Paper 2009-4856, July 2009.

[7] Wang, T.-S., "Transient Three-Dimensional Startup Side Load Analysis of a Regeneratively Cooled Nozzle," *Shock Waves*, Vol. 19, No. 3, 2009, pp. 251–264. doi:10.1007/s00193-009-0201-2

[8] Wang, T.-S., and Guidos, M., "Transient Three-Dimensional Side Load Analysis of a Film-Cooled Nozzle," *Journal of Propulsion and Power*, Vol. 25, No. 6, 2009, pp. 1272–1280. doi:10.2514/1.41025

[9] Ostlund, J., and Bigert, M., "A Sub Scale Investigation Side Loads in Sea Level Rocket Nozzles," AIAA Paper 99-2759, June 1999.

[10] Ostland, J., "Supersonic Flow Separation with Application to Rocket Engine Nozzles," Ph.D. Thesis, Royal Institute of Technology, Stockholm, 2004.

[11] Deck, S., "Delayed Detached Eddy Simulation of the End-Effect Regime and Side-Loads in an Overexpanded Nozzle Flow," *Shock Waves*, Vol. 19, No. 3, 2009, pp. 239–249. doi:10.1007/s00193-009-0199-5

[12] Hadjada, A., and Onofri, M., "Nozzle Flow Separation," *Shock Waves*, Vol. 19, No. 3, 2009, pp. 163–169. doi:10.1007/s00193-009-0209-7

[13] Tomita, T., Takahashi, M., Sasaki, M., Sakamoto, H., Takahashi, M., and Tamura, H., "Experimental Evaluation of Side Loads in LE-7A Prototype Engine Nozzle," *Shock Waves*, Vol. 19, No. 3, 2009, pp. 213–228. doi:10.1007/s00193-009-0191-0

[14] Nguyen, A. T., Deniau, H., Girard, S., and De Roquefort, T. A., "Unsteadiness of Flow Separation and End-Effects Regime in a Thrust-Optimized Contour Rocket Nozzle," *Flow, Turbulence and Combustion*, Vol. 71, 2003, pp. 161–181. doi:10.1023/B:APPL.0000014927.61427.ad

[15] Deck, S., and Guillen, P., "Numerical Simulation of Side loads in an Ideal Truncated Nozzle," *Journal of Propulsion and Power*, Vol. 18, No. 2, 2002, pp. 261–269. doi:10.2514/2.5965

[16] Shimizu, T., Miyajima, H., and Kodera, M., "Numerical Study of Restricted Shock Separation on a Compressed Truncated Perfect Nozzle," *AIAA Journal*, Vol. 44, No. 3, 2006, pp. 576–584. doi:10.2514/1.14288

[17] Kwan, W., and Stark, R., "Flow Separation Phenomena in Subscale Rocket Nozzles," AIAA Paper 2002-4229, July 2002.

[18] Reijasse, Ph., and Boccaletto, L., "Influence of Film Cooling on Nozzle Side loads," AIAA Paper 2008-392, Jan. 2008.

[19] Wang, T.-S., "Multidimensional Unstructured-Grid Liquid Rocket Engine Nozzle Performance and Heat Transfer Analysis," *Journal of Propulsion and Power*, Vol. 22, No. 1, Jan.–Feb. 2006, pp. 78–84. doi:10.2514/1.14699

[20] Shang, H. M., and Chen, Y.-S., "Unstructured Adaptive Grid method for Reacting Flow Computation," AIAA Paper 1997-3183, July 1997.

[21] Wang, T.-S., Chen, Y.-S., Liu, J., Myrabo, L. N., and Mead, F. B., Jr., "Advanced Performance Modeling of Experimental Laser Lightcraft," *Journal of Propulsion and Power*, Vol. 18, No. 6, 2002, pp. 1129–1138. doi:10.2514/2.6054

[22] Chang, G., Ito, Y., Ross, D., Chen, Y.-S., Zhang, S., and Wang, T.-S., "Numerical Simulations of Single Flow Element in a Nuclear Thermal Thrust Chamber," AIAA Paper 2007-4143, June 2007.

[23] Chen, Y.-S., and Kim, S. W., "Computation of Turbulent Flows Using an Extended k-ε Turbulence Closure Model," NASA CR-179204, Oct. 1987.

[24] Wang, T.-S., Droege, A., D'Agostino, M., Lee, Y.-C., and Williams, R., "Asymmetric Base-Bleed Effect on X-33 Aerospike Plume Induced Base-Heating Environment," *Journal of Propulsion and Power*, Vol. 20, No. 3, 2004, pp. 385–393. doi:10.2514/1.10385

[25] Chen, Y.-S., Cheng, G. C., and Farmer, R. C., "Reacting and Non-Reacting Flow Simulation for Film Cooling in 2-D Supersonic Flows," AIAA Paper 92-3602, July 1992.

[26] Wang, T.-S., Canabal, F., Chen, Y.-S., and Cheng, G. C., "Multiphysics Computational Analysis of a Solid-Core Nuclear Thermal Engine Thrust Chamber," *Journal of Propulsion and Power*, Vol. 26, No. 3, May–June 2010, pp. 407–414. doi:10.2514/1.47759

[27] Svehla, R. A., and McBride, B. J., "FORTRAN IV Computer Program for Calculation of Thermodynamic and Transport Properties of Complex Chemical Systems," NASA TN D-7056, Jan. 1973.

[28] Steinbrenner, J. P., Chawner, J. R., and Fouts, C., "Multiple Block Grid Generation in the Interactive Environment," AIAA Paper 90-1602, June 1990.

[29] Tomita, T., Takahashi, M., Sasaki, M., Takahashi, M., Tamura, H., Watanabe, Y., and Tsuboi, M., "Parametric Study on the Influence of a Discontinuous Step in a Nozzle Contour on Side-Load," AIAA Paper 2003-4764, July 2003.

[30] Wonezawa, K., Yokota, K., Tsujimoto, K., Sakazume, N., and Watanabe, Y., "Three-Dimensional Unsteady Flow Simulation of Compressed Truncated Perfect nozzles," AIAA Paper 2002-3991, July 2002.

K. Frendi
Associate Editor